AIP Journal of Applied Physics

Combined effects of vertical and lateral confinement on the magnetic properties of MnAs micro and nano-ribbons

L. B. Steren, M. Tortarolo, F. Fernandez Baldis, M. Sirena, M. Sacchi, V. H. Etgens, M. Eddrief, B. Santos, T. O. Mentes, and A. Locatelli

Citation: Journal of Applied Physics **120**, 093905 (2016); doi: 10.1063/1.4961501
View online: http://dx.doi.org/10.1063/1.4961501
View Table of Contents: http://scitation.aip.org/content/aip/journal/jap/120/9?ver=pdfcov
Published by the AIP Publishing

Combined effects of vertical and lateral confinement on the magnetic properties of MnAs micro and nano-ribbons

L. B. Steren,[1,2] M. Tortarolo,[1,2] F. Fernandez Baldis,[2,3] M. Sirena,[2,3] M. Sacchi,[4,5] V. H. Etgens,[6] M. Eddrief,[4,5] B. Santos,[7] T. O. Mentes,[7] and A. Locatelli[7]
[1]*Centro Atómico Constituyentes CNEA, 1650 San Martín, Argentina*
[2]*Consejo Nacional de Investigaciones Científicas y Técnicas, C1033AAJ Buenos Aires, Argentina*
[3]*Centro Atómico Bariloche and Instituto Balseiro, CNEA, 8400 S. C. de Bariloche, Argentina*
[4]*Sorbonne Universités, UPMC Univ. Paris 06, UMR 7588, INSP, 4 place Jussieu, F-75005 Paris, France*
[5]*CNRS, UMR 7588, Institut des Nanosciences de Paris, 4 place Jussieu, F-75005 Paris, France*
[6]*Fédération Lavoisier Franklin, UVSQ, 78035 Versailles Cedex, France*
[7]*Elettra-Sincrotrone Trieste S.C.p.A., 34149 Basovizza, Trieste, Italy*

(Received 5 July 2016; accepted 10 August 2016; published online 7 September 2016)

The micromagnetic domain structure of MnAs films gave place to an intense research activity in the last few years due to its potential application in magneto-electronic devices such as domain-wall track memories and logic circuits. These applications require a full knowledge of miniaturization effects on the magnetic properties of the material. In this work, X-ray photoemission electron microscopy has been used for imaging magnetic domains in lithographically fabricated MnAs ribbons, addressing the dependence of the domain configuration on film thickness and ribbon width. Our experiments show a transition from head-on to regular stripe domains below a critical width/thickness ratio $w_c \approx 6$. Micromagnetic simulations suggest that this transition is correlated to the magnetic structure of the surface plane. Depending on the ribbon width and thickness, the magnetic configuration is shown to evolve from flux-closure domain structure to a state of almost homogeneous magnetization, observed for narrower ribbons. The evolution of the domain structure, magnetic fraction, and magnetization with temperature has been studied across the ferromagnetic/paramagnetic transition. Our experiments show that the magnetic configuration in ribbons exhibits higher stability to temperature variations than in as-cast films. *Published by AIP Publishing.*
[http://dx.doi.org/10.1063/1.4961501]

I. INTRODUCTION

The potential of magnetic semiconductors for developing magnetocaloric[1] and spintronic[2–4] devices has recently spurred the research activity in MnAs films. Characterizing and understanding the magnetic configuration of MnAs mesoscopic structures have thus become an essential clue for device design.

Bulk MnAs[5] exhibits a first-order magneto-structural transition above room temperature that drives the system from a hexagonal ferromagnetic (FM) phase (α) to an orthorhombic paramagnetic phase (β). In MnAs thin films, the α and β phases coexist over a rather wide temperature range below T_C.[6,7] The crystal orientations of film and substrate determine the geometrical arrangement of the α and β phases in the coexistence regime (CR). In the case of MnAs/GaAs (001) and other $[1\bar{1}00]$ oriented films, the α and β phases form a stripe pattern where ferromagnetic (FM) ridges alternate with paramagnetic grooves along the MnAs [0001] direction (c-axis). The period λ of the stripes and the height h of the ridges increase almost linearly with the film thickness, t.[8]

The strong crystal-field interaction arisen in the MnAs hexagonal structure produces a large uniaxial magneto-crystalline anisotropy (MC),[9] with the hard-axis oriented parallel to [0001]. The MnAs anisotropy constant, $K_{uniax} \sim 0.7\,MJ/m^3$, is comparable to those of permanent magnets.[10] The magnetic properties of MnAs films are highly sensitive to film thickness and substrate orientation.[11] Extensive work has been done to characterize the domain structure of these films.[12] A variety of domain types can be observed as a function of temperature in MnAs/GaAs(001) films, depending on the thickness and the α-stripe width.[13] The large MC anisotropy and demagnetizing fields ensure that all magnetic domains are aligned along the $[11\bar{2}0]$ easy axis (a-axis) at the surface of thin films for $t > 10\,nm$.[14] The simplest domain configuration observed in the demagnetized state in a-stripes are slabs oriented in both sense of the easy direction along the magnetic stripe, having the same width of the stripes. In the demagnetized state, the simplest domains observed in α-stripes are slabs oriented in both sense of the easy direction along the magnetic stripe, having the same width of the stripes. Other domains are composed of two or three head-on subdomains, all oriented along the easy direction within the ferromagnetic stripe. Due to the effect of demagnetizing fields, the out-of-plane direction is an intermediate[9] axis, and consequently, domain reversal exhibits 180° Bloch walls. X-ray magnetic circular dichroism photoemission electron microscopy (XMCD-XPEEM) confirmed the domain structures observed by magnetic force microscopy (MFM) while providing a deeper insight into the properties of the patterns.[15]

MnAs properties are affected by vertical confinement as demonstrated by studies performed on thin films. The change of the domain patterns with temperature in the α–β phase coexistence regime (CR) has been shown to be remarkable.[16] Engel-Herbert and Hesjedal examined the evolution of

MnAs domain structure with film thickness, finding a transition from three-dimensional flux-closure to single-domain states for films thinner than 120 nm.[14] A recent study performed on MnAs nano-disk arrays showed that the CR is affected by the structures' size as it approaches the nanoscale.[17] Size effects were also reported in other studies on the magnetic properties of MnAs micro and nanoribbons.[18,19] Despite these efforts, it is not yet possible to draw a complete picture of the ribbon magnetism. An exhaustive characterization complemented by simulations is clearly necessary to reveal the magnetic domain characteristics in the FM phase and also at the CR.

Here, we investigate the influence of the lateral and vertical dimensions of MnAs ribbons on their magnetic domain configuration by means of XMCD-XPEEM imaging. We analyze the size and shape of domains as a function of the transverse cross-section dimensions and crystallographic orientation. One of the aims of our work is to evaluate the formation of regular patterns in the ribbons, depending on the parameters such as aspect ratio, thickness, and ribbon orientation. In fact, the characteristics are particularly important for future applications in Domain Wall (DW) based memory devices.

Moreover, imaging the ribbon domain structure through the magnetic phase transition makes it possible to simultaneously determine the evolution of the α phase fraction and of the magnetization as a function of temperature. The experiments are complemented by micromagnetic simulations, which give a deeper knowledge of three-dimensional domains.

II. EXPERIMENTAL DETAILS

Ribbons of different size and crystallographic orientation were prepared by e-beam lithography followed by Ar ion milling on 50 nm and 30 nm thick MnAs films grown by molecular beam epitaxy (MBE) on GaAs(100) substrates following the procedure described previously.[9] The films were capped with a thin GaAs layer to avoid oxidation. Prior to the XMCD-XPEEM imaging, the samples were decapped *in situ* by Ar-etching. After sputtering, the samples were heated in UHV up to about 350 °C, in order to restore crystalline order. To avoid partial lifting of the MnAs films, the removal of the capping GaAs layer was monitored by the x-ray absorption intensity at the MnL_3 edge.

The ribbons were all 20 μm long, with their long axis either parallel or perpendicular to the MnAs [0001] direction (see Fig. 1). The ribbons width w varied from 0.2 μm to 5 μm. The samples were indexed as $S_{w\text{–PA(PE)}}$–t where PA(PE) indicates the parallel (perpendicular) orientation of l with respect to [0001] and t is the thickness of the films.

Reference 30 nm and 50 nm thick MnAs/GaAs(100) films were characterized using a superconducting quantum interference device magnetometer (SQUID). The magnetization of these samples lay in the plane of the films with the hard-axis oriented along the MnAs [0001] direction.

The XMCD-PEEM measurements were carried out using the SPELEEM microscope at the undulator beamline Nanospectroscopy[20] of the Elettra storage ring in Trieste, Italy. This instrument can perform x-ray absorption spectroscopy (XAS) and XMCD-PEEM measurements, achieving routinely a lateral resolution of ~30–40 nm.[21] The XMCD images shown here were obtained by acquiring secondary photoemission images at the Mn L3 edge with opposite photon helicity and performing the following image arithmetic, pixel by pixel: $I_{XMCD} = (I_- - I_+)/(I_- + I_+)$, where I_- and I_+ correspond to the intensity of the images acquired with negative and positive helicities. In our measurements, the MnAs samples were positioned onto a Mo plate, which was kept in close contact with a Mo ring onto which a C type thermocouple was spot-welded. The sample temperature was varied in the range from −10 °C to 70 °C.

A magnetic field of 2.5 kOe applied parallel to the easy-axis was employed to saturate the samples at low temperature. Once saturated, the samples were heated until reaching the paramagnetic state and cooled down again to the ferromagnetic state to study the magnetic domain structures in both saturated and remnant states. The micromagnetic simulations were performed using the MuMax3 package.[22] The simulation parameters for MnAs were taken from Ref. 14: exchange stiffness constant $A = 1 \times 10^{-11}$ J/m, saturation magnetization $M_S = 8 \times 10^5$ A/m, and magnetocrystalline anisotropy constant $K = -7.2 \times 10^5$ J/m^3. The calculations were performed at zero temperature, not taking into account the effects of thermal fluctuations.

III. RESULTS AND DISCUSSION

A. Magnetic domain configuration

1. Lateral and vertical confinement

XPEEM images of the typical domain structure of the ribbons are shown in Fig. 2, as a function of the ribbon width and orientation. In all cases, the domains are oriented along the

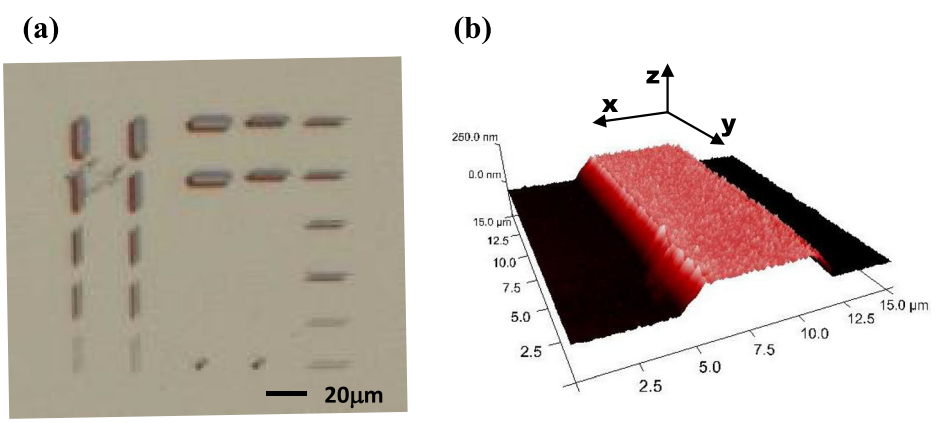

FIG. 1. (a) Layout of the microfabricated MnAs ribbons patterned along mutually perpendicular crystallographic axes and (b) AFM scan of a $S_{5\text{-PE}}$-50 ribbon.

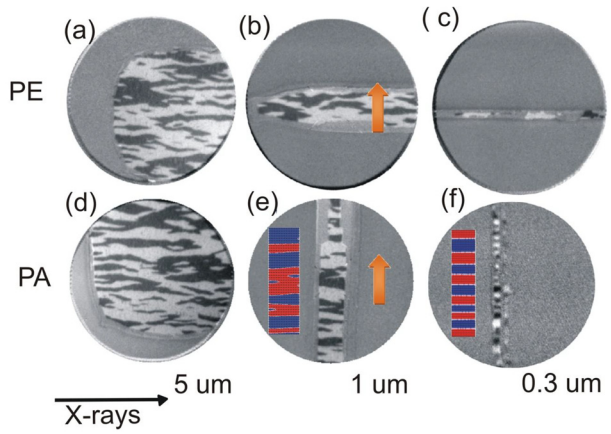

FIG. 2. XPEEM images of (a) $S_{5\text{-PE}}$-30, (b) $S_{1\text{-PE}}$-30, (c) $S_{0.2\text{-PE}}$-30, (d) $S_{5\text{-PA}}$-30, (e) $S_{1\text{-PA}}$-30, and (f) $S_{0.3\text{PA}}$-30, measured at 25 °C in remnant state. Arrows indicate [0001] direction. Field of view: 5 μm.

MnAs easy-axis, pointing either in the direction parallel and antiparallel to it (black and white contrast, respectively). The type of the domains observed in thin ribbons is different from those found in thick films ($t > 100$ nm). Wedge shaped domains elongated along the easy-axis direction were observed at temperatures below T_c for wider 30 nm and 50 nm thick-ribbons. This kind of pattern is known to develop in thin ferromagnetic films with strong uniaxial in-plane anisotropy in order to reduce the magnetic charge density when the magnetization of two adjacent domains meets head-on.[23] A transition between head-on domains and a regularly stack of open stripe-domain states is observed as the ribbons become narrower. The boundary between both configurations is set by the ribbon aspect ratio w/t. A detailed discussion of this result will be given in Section III A 2. The observation of domain walls is limited by the XPEEM lateral resolution.

The analysis of the domain sizes and the wedge angle in wide ribbons, $w/t > 10$, provides additional information about the domain structure. A qualitative look at the images shows that thinner ribbons have a larger number of domains together with a larger distribution of sizes and wedge angles (Fig. 3). A quantitative description of the domain size distribution along the ribbons was deduced from analysis of the frequency histograms of the domain width, D, measured along the [0001] direction (Fig. 4(a)). Both $S_{w\text{–PA}}$ and $S_{w\text{-PE}}$ ribbons present similar characteristics. The average domain width $\langle D \rangle$ for ribbons of different widths and thicknesses is shown in Fig. 4(b). As can be appreciated by a visual inspection of the XPEEM images, the mean width $\langle D \rangle$ of the 50 nm-thick ribbons is larger than those of 30 nm-thick ones, and increases from 0.17 μm to 0.56 μm with the ribbon width. Instead, in 30 nm-thick ribbons $\langle D \rangle$ remains nearly constant at 0.2 μm and exhibits a wider distribution size. The broader ribbons behave as continuous thin films. As their thickness decreases, they exhibit a larger split of domains whose average size decreases.[24,25] These results are understood by noting that in these ribbons, the domain size is smaller than the ribbons width but larger than their thickness.

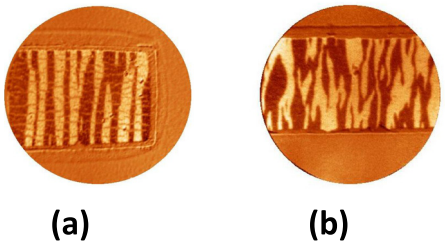

FIG. 3. XPEEM images of (a) $S_{5\text{-PA}}$-50 and (b) $S_{5\text{-PA}}$-30, measured at room temperature in remnant state.

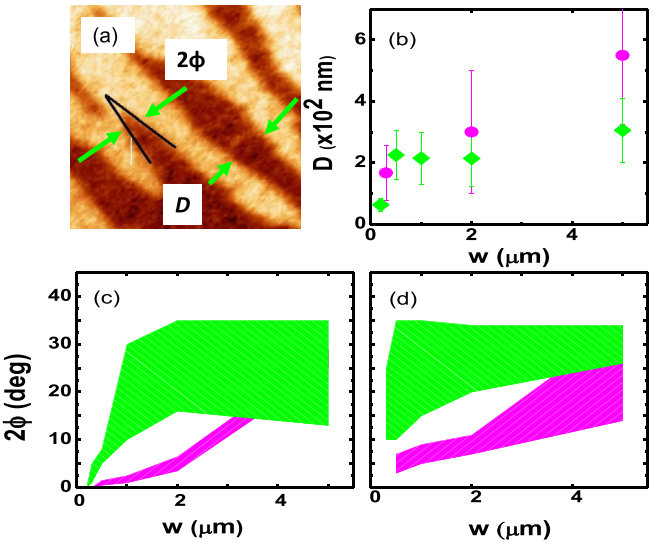

FIG. 4. (a) Details of a XPEEM typical image corresponding to a $S_{5\text{-PA}}$-30 MnAs ribbon measured at room temperature where the angle at the edge of head-on domains, 2ϕ, and the domain size D are indicated. (b) Domain size D as a function of ribbons width w measured along the c-axis for (●) $S_{w\text{-PA}}$-50 and (◆) $S_{w\text{-PA}}$-30 ribbons. (c and d) 2ϕ angle distribution as a function of the ribbons width w, for (c) $S_{w\text{-PA}}$ and (d) $S_{w\text{-PE}}$ ribbons. Green \\\ (magenta ///) shaded areas correspond to 30 nm (50 nm)-thick ribbons.

The angle at the edge of the head-on domains (Fig. 4(a)) has been also examined and plotted in Figs. 4(c) and 4(d) for $S_{w\text{-PA}}$ and $S_{w\text{-PE}}$ samples, respectively. The patterned area is associated to $\langle 2\phi \rangle \pm \sigma$ intervals, evaluated for each ribbon's width and thickness. The \\\ (///) pattern corresponds to 30 nm-thick (50 nm-thick) structures. As can be noticed from the image, the wedge angles depend on the ribbon thickness. While the average $\langle 2\phi \rangle$ remains almost constant around $\langle 2\phi \rangle_{30} = 25°$ down to $w = 1$ μm for 30 nm-thick ribbons, it decreases almost linearly to zero for the thicker ones. Wedge boundaries are formed in order to reduce the magnetostatic energy and magnetic charge density. The saw-tooth angle 2ϕ is determined by the competition between the domain wall and dipolar energies. For thin films,[23,24] $2\phi = \gamma w/4M_S t$ where γw is the domain wall energy and M_S is the saturation magnetization of the sample. The type of domain walls is similar for all the samples according to micromagnetic simulations (see Section III A 2) so we do not expect any functional change of γw with the anisotropy and the exchange stiffness constants. The variation of the wedge angle with the ribbons width for 50 nm-thick structures would mean that the effective anisotropy changes as w varies. Our simulations indicate that the width of the walls varies between 50 nm and 80 nm in $S_{w\text{-PA}}$–50 and $S_{w\text{-PA}}$–30 samples, respectively, which is comparable to the film thickness and is in agreement with Shippan Dennis and coworkers.[25,26] The larger

effect of lateral confinement on the wedge angle and domain sizes in 50 nm-thick larger ribbons would indicate a critical size of the structures. Below this film thickness, the effect of surfaces would dominate the magnetic domain properties and so the variation of the size parameters does not affect significantly.

2. Dependence on the aspect ratio w/t

The shape and size of the domains do not change with w/t for ribbons aligned perpendicular to the MnAs c-axis ($S_{w\text{-PE}}$). Instead, in $S_{w\text{-PA}}$ the wedge-shape (Fig. 2(d)) domains turn into a regular stacking of anti-parallel domains with homogeneous magnetization across the width of the ribbons and oriented parallel to the easy-axis below a critical aspect ratio $w/t \sim 6$, as seen in the experiments (Figs. 2(e) and 2(f)). In order to get a deeper understanding of our experimental results, micromagnetic simulations[23] were performed on a large variety of S_{PA} samples: thicknesses varying from $t = 10$ nm to 160 nm and widths ranging from $w = 10$ nm up to 1000 nm. The surface magnetic domain configuration measured by XMCD-PEEM is related to the x-y plane view magnetic configuration of the ribbons.[20] Our simulations reproduce the progressive variation of the domain arrangement with w/t observed in our measurements and provide additional information about the domain structure phases for $0 \leq \boldsymbol{w/t} \leq 35$ and $10\,\text{nm} \leq \boldsymbol{t} \leq 160\,\text{nm}$. The domains were classified into six different phases, identified from I to VI (Figure 5(a)), taking into account the domain shapes (Figure 5(b)), the magnetization uniformity along the ribbons thickness, y-z plane (Figure 5(c)), and domain wall types in the x-z easy plane (Figure 5(d)).

The competition of the strong uniaxial anisotropy of MnAs together with the shape anisotropy of the structures

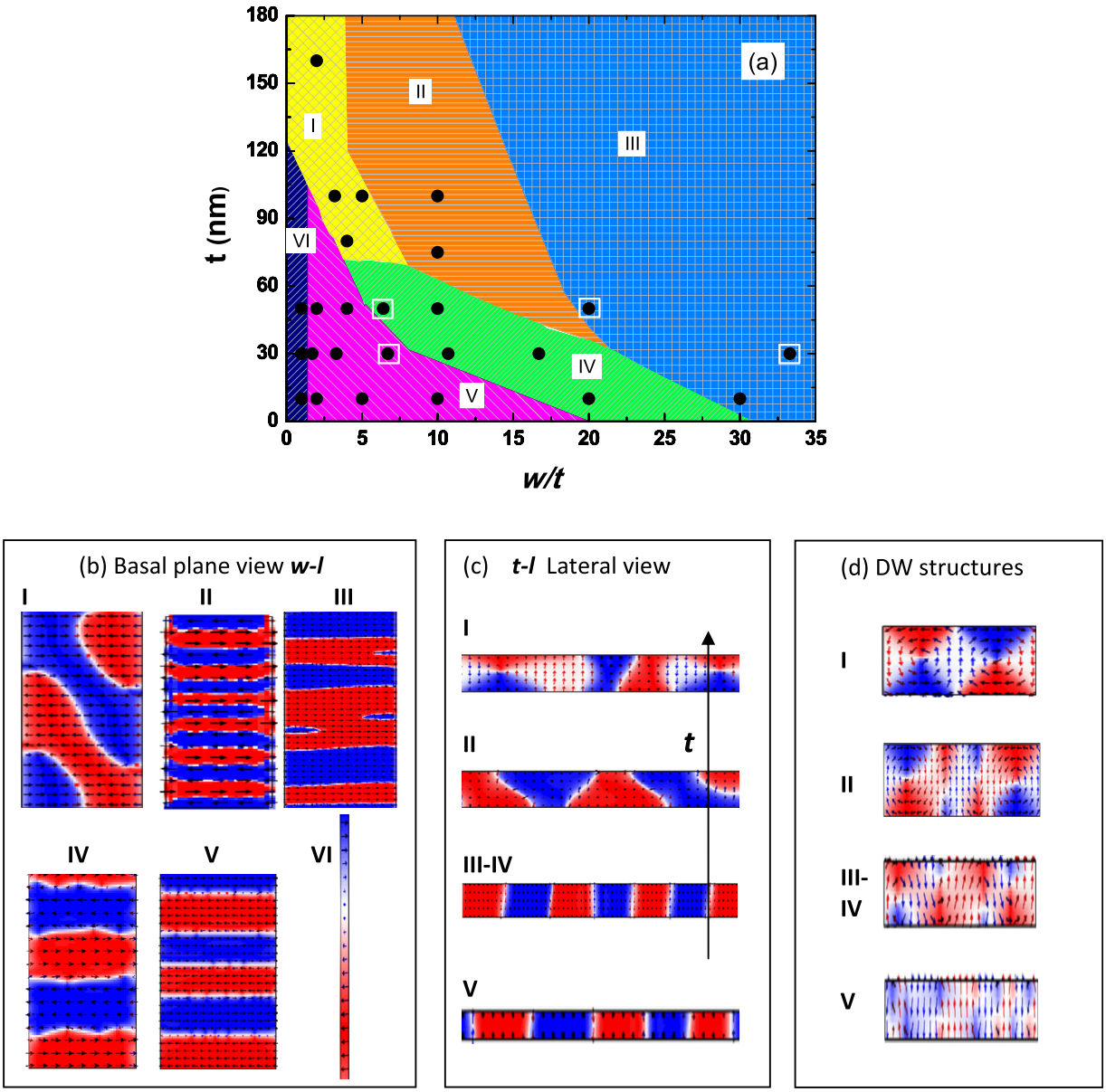

FIG. 5. (a) Phase diagram of MnAs $S_{w\text{-PA}}$-t ribbons of various thicknesses (from $t = 10$ nm to 160 nm) and $\boldsymbol{w/t}$ ranging from 1 up to 35. The dots correspond to the simulated configurations. The samples studied experimentally are indicated by squares. Boundaries between different colored regions separate different domains and/or DW structures (I → VI). (b) Surface magnetization; (c) domain structure in the cross-sectional y-z plane of ribbons with different thickness—increasing from bottom to top; and (d) examples of different domain wall types observed along the x-y easy plane.

determines that, for $w/t \geq 2$, the magnetization is aligned along the *x*-axis (for PA geometry, along the ribbons width). The DW-type depends not only on the ***w/t*** ratio but also on the structures' thickness. As reported in Ref. 20 for thin films, three-dimensional arrangement of magnetic states (Fig. 5(a)-region I), i.e., Landau, diamond, and double-diamonds, is observed for $2 \leq \boldsymbol{w/t} \leq 4$ and thickness varying from 160 nm down to 80 nm. In this region, the DWs are typically rounded in the *x*-*y* plane, separating head-on domains. The development of these kinds of flux closure structures allows to reduce the demagnetizing energy arising when two domains meet head on, thus stabilizing the straight boundaries and wedge structures on the surface of the sample (see Fig. 5(b-I) and upper image of Fig. 5(c)). As the width of the structures broadens (Fig. 5(a)-region II), the shape anisotropy forces the magnetization to lie uniformly in the plane of the ribbons. The boundaries between domains are still rounded at the surface of the ribbons and tilted along the *z*-axis (see Fig. 5(b-II) and second image of Fig. 5(c) from the top). The DWs at the cross-sectional *x*-*z* easy plane are composed of Bloch lines with vortex substructures that serve to reduce stray fields[26] (Fig. 5(d)). In broad but thinner ribbons, the magnetic domains become wedges in the *x*-*y* plane (Fig. 5(a)-region III). This kind of wedge structure was observed by XPEEM for $w/t \sim 150$ to 20 and corresponds to images shown in Figs. 2(a), 2(b), 2(d), and 2(e). As the thickness decreases, the DWs straighten along the *x*-direction (Fig. 5(a)-region IV; Fig. 5(b); Fig. 5(c) third image from the top) and become completely aligned for $6 \leq \boldsymbol{w/t} \leq 10$ (Fig. 5(a)-region V; Fig. 5(a); Fig. 5(c) image at the bottom)). These structures correspond to the experimental images in Figs. 2(c) and 2(f): the ribbons present simple domains. For $w/t \sim 1$ (Fig. 5-region VI), there is a coexistence of in-plane and out-of-plane magnetized domains, separated by Bloch and vortex DW.

Despite the fact that both the domain shape and DW-type are similar for 50 nm and 30 nm-thick structures, subtle differences are observed in the micromagnetic simulations. However, the phase boundaries between III, IV, and V for samples with these thicknesses are essentially defined by the ***w/t*** ratio. The DWs are composed of Bloch lines alternated with different substructures (Fig. 5(d)). Walls and lines are of comparable sizes for $S_{500\text{-PA}}$–50 ribbons, while the Bloch lines are ultrathin for $S_{500\text{-PA}}$–30 ones. As the width of the samples is reduced, this tendency is kept. For $2 \leq \boldsymbol{w/t} \leq 6$ and thin structures, the DWs broaden and so the Bloch lines. In this aspect ratio range, the effective demagnetizing factor Nx decreases to 0.5, affecting notably the orientation of the magnetization within the domain. Progressively, the out-of-plane component of the magnetization increases with decreasing ***w/t***.

B. Temperature dependence of the sample magnetization and ferromagnetic fraction

As can be seen in Fig. 6, the remnant micromagnetic structure does not show significant changes as the temperature increases from low temperature to T_C. The XPEEM images of the thicker ribbons show a progressive loss of magnetic contrast as the samples are heated from low

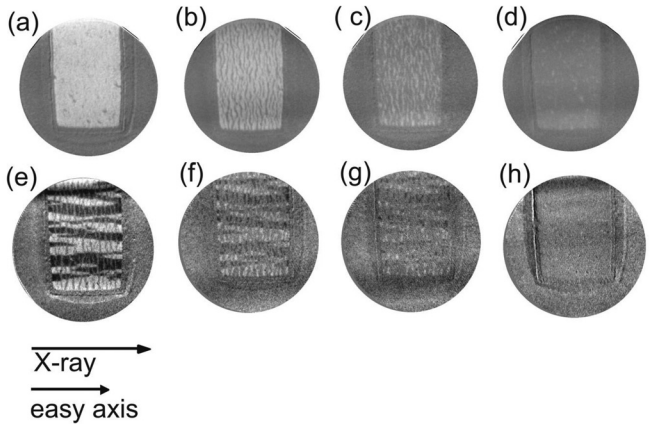

FIG. 6. XPEEM images of the $S_{5\text{-PA}}$-50 ribbons measured in saturated (a)–(d) and remnant (e)–(h) states at different temperatures: (a) $T = -10\,^{\circ}C$, (b) $T = 22\,^{\circ}C$, (c) $T = 32\,^{\circ}C$, (d) $T = 48\,^{\circ}C$, (e) $T = 20\,^{\circ}C$, (f) $T = 32\,^{\circ}C$, (g) $T = 40\,^{\circ}C$, and (h) $T = 48\,^{\circ}C$. Field of view: 10 μm.

temperature, but the overall domain pattern within the α stripes is preserved even at high temperatures. No effect was observed as the temperature was increased, even for a β phase width of the order of ~250 nm close to T_C. Ribbon domains seem to be more stable than those of films, where a progressive decoupling is observed together with a change of the domain pattern[19] as the ferromagnetic stripes become narrower and separated by β ones.

We were not able to resolve the presence of β-stripes in the thinner ribbons (not shown). However, an anisotropic behaviour related to the existence of stripes was appreciated in transport measurements and reported recently.[27] It has to be noted that according to Ref. 8, the α/β period should be $\lambda_e = 144$ nm and the height of the FM ridges $h = 0.3$ nm for $t = 30$ nm films. Moreover, an earlier work[28,29] showed that the long-range order of α/β stripes along the films is lost for films thinner than 50 nm, and only bunches of short stripes are observed by MFM in saturated MnAs films. Hence, this lack of long-range order could explain the difficulty of observing any feature of the α/β stripes array in XPEEM images of $Sw_{PA(PE)}$-30 ribbons.

We have determined from the XPEEM measurements the variation of the α fraction of the MnAs phase, ξ, with temperature for the S_{5PAR}–50 sample (Fig. 7). This parameter was directly estimated from the images, calculating the surface occupied by magnetic regions normalized to the total sample surface. The evaluation of the ξ-temperature dependence was done by heating the samples from both the saturated and remnant states, respectively. The ferromagnetic fraction decreases above 7 °C, following a T^2 law until ~30 °C and drops towards the Curie temperature ($T_C \sim 43\,^{\circ}C$), although the progressive decrease in the magnetic contrast makes it difficult to determine the phase fraction when approaching the T_C. The behavior reported in this manuscript differs from the results obtained in thin films by X-ray diffraction spectroscopy.[9] The authors found a quasi-linear dependence of ξ with temperature in a narrow temperature interval ($\Delta T \sim 10$ K). We believe that the qualitative difference of the temperature behavior of ξ lies on the fact that the phase coexistence is examined at different stages and with a different resolution. Moreover, while

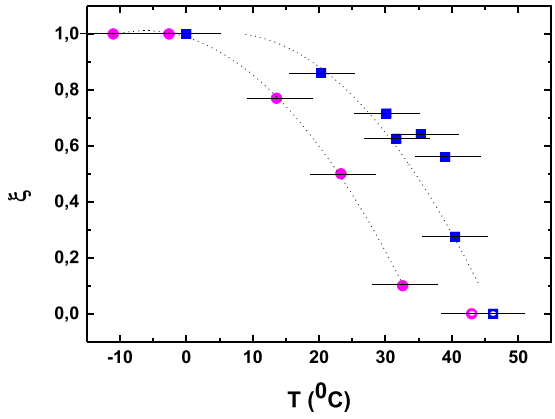

FIG. 7. α-phase fraction, ξ, as a function of temperature, determined from XPEEM images of $S_{5\text{-}PA}$-50 ribbon. Both series of data were obtained while heating the sample from low temperature in different magnetic states: (●) saturated and (■) remnant states, respectively. The two curves are shifted due to differences in the thermal contact between the sample and the support, a Mo ring onto which a WRe type S thermocouple is spot-welded.

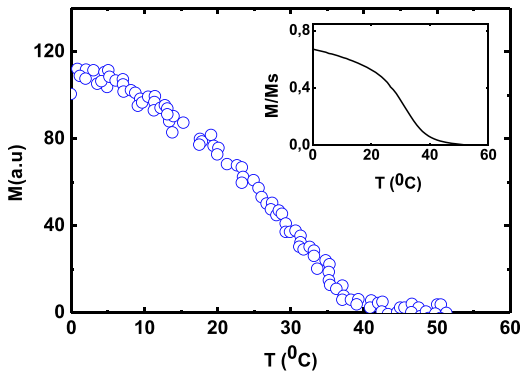

FIG. 8. Magnetization vs. temperature plot, deduced from the XPEEM images contrast for a S_{5PAR}-50 ribbon. Inset: magnetization curve measured for a 50 nm-MnAs film. Absolute temperatures are measured with an uncertainty of about 20 °C.

XPEEM is only sensitive to the sample surface, XRD gives an average measure over the bulk of the sample.

The temperature dependence of the magnetization of the ferromagnetic phase has been analyzed by quantifying the change of magnetic contrast of α zones as a function of temperature. In Fig. 8, the magnetization vs. temperature curve extracted from the XPEEM images is shown for the 50 nm sample. As a reference, the magnetization of 50 nm thin films is plotted in the inset. The comparison between the magnetization of the films and the ribbons shows differences in the behavior of the demagnetization process. In the thin film, the curve is quite similar to the bulk material, governed by the ferro-paramagnetic first-order phase-transition. It has to be noted that the magnetization curves, measured by SQUID, account not only for the change of the magnetization of the α phase with temperature but also for the decrease of the α phase fraction with increasing temperature.

IV. CONCLUDING REMARKS

We used XPEEM to image the magnetic domain structures of rectangular micro and nano ribbons lithographed in 30 nm and 50 nm thick MnAs films confined along different crystallographic axes. The direct analysis of the shape (wedge angle) and size of the magnetic domains suggests that there is a critical thickness below which the surface effects would dominate over the magnetic domain properties and so the variation of the size parameters does not affect the domains' size and shape significantly. On the one hand, the magnetic domains in samples confined along the c-axis do not show significant change when their size is reduced. On the other hand, samples confined along the a-axis present a transition from head-on domains to regularly stacked rectangular domains for the aspect ratio $w/t \sim 6$. Our simulations showed that this transition is correlated with the formation of flux closure structures on the *x-y* surface of the ribbon that allow to decrease the magnetostatic energy in head-on domains when the ribbons are wide enough. This behavior is ascribed to the balance between shape and magneto-crystalline anisotropies. The magnetic domains' shape and size are stable with respect to temperature. We have shown that it is possible to control the development of regular domain patterns in MnAs ribbons by a careful choice of their width, thickness, and orientation.

Finally, the change of ferromagnetic fraction and magnetization with temperature was estimated by analyzing independent parameters, showing that magnetic domains' shape and size are stable with respect to temperature and that the magneto-thermal history of the sample plays a role in the development of the coexistence regime.

In summary, we have shown that the MnAs mesoscopic structures exhibit a rich variety of magnetic domain structures that can be tuned by adjusting their size and orientation. These characteristics are extremely promising for its future application in DW-based devices, such as memories and logic circuits.

ACKNOWLEDGMENTS

L.B.S., M.T., F.F.B., V.H.E., M.E., and M.S. are members of the Laboratorio Internacional Franco-Argentino en Nanociencias (LIFAN). We acknowledge the partial financial support from the PICT Contract No. 03/1187, CONICET Grant No. PIP 112-201101-00482, and Elettra. L.B.S. and F.F.B. acknowledge the support from the ICTP-Elettra Users Programme by Grant No. 20120129. We thank J. P. Sinnecker for his valuable contribution on micromagnetic simulations and M. Marangolo for fruitful discussions.

[1]J.-Y. Duquesne, J.-Y. Prieur, J. A. Canalejo, V. H. Etgens, M. Eddrief, A. L. Ferreira, and M. Marangolo, Phys. Rev. B **86**, 035207 (2012).
[2]M. E. Nowakowski, G. D. Fuchs, S. Mack, N. Samarth, and D. D. Awschalom, Phys. Rev. Lett. **105**, 137206 (2010).
[3]C. Spezzani, E. Ferrari, E. Allaria, F. Vidal, A. Ciavardini, R. Delaunay, F. Capotondi, E. Pedersoli, M. Coreno, C. Svetina, L. Raimondi, M. Zangrando, R. Ivanov, I. Nikolov, A. Demidovich, M. B. Danailov, H. Popescu, M. Eddrief, G. De Ninno, M. Kiskinova, and M. Sacchi, Phys. Rev. Lett. **113**, 247202 (2014).
[4]M. Tortarolo *et al.*, Appl. Phys. Lett. **101**, 072408 (2012).
[5]C. P. Bean and D. S. Rodbell, Phys. Rev. **126**, 104 (1962).
[6]V. M. Kaganer, B. Jenichen, F. Schippan, W. Braun, L. Däweritz, and K. H. Ploog, Phys. Rev. B **66**, 045305 (2002).
[7]L. Daweritz, Rep. Prog. Phys. **69**, 2581 (2006).

[8]R. Breitwieser, F. Vidal, I. L. Graff, M. Marangolo, M. Eddrief, J.-C. Boulliard, and V. H. Etgens, Phys. Rev. B **80**, 045403 (2009).
[9]L. B. Steren, J. Milano, V. Garcia, M. Marangolo, M. Eddrief, and V. H. Etgens, Phys. Rev. B **74**, 144402 (2006).
[10]J. A. C. Bland and B. Heinrich, *Ultrathin Magnetic Structures I* (Springer, 1994).
[11]R. Engel-Herbert, T. Hesjedal, J. Mohanty, D. M. Schaadt, and K. H. Ploog, Phys. Rev. B **73**, 104441 (2006).
[12]R. Engel-Herbert, T. Hesjedal, and D. M. Schaadt, Phys. Rev. B **75**, 094430 (2007).
[13]R. Engel-Herbert, T. Hesjedal, J. Mohanty, D. M. Schaadt, and K. H. Ploog, J. Appl. Phys. **98**, 063909 (2005).
[14]R. Engel-Herbert and T. Hesjedal, J. Magn. Magn. Mater. **323**, 1840 (2011).
[15]L. Däweritz, D. Kolovos-Vellianitis, A. Trampert, C. Herrmann, K. H. Ploog, E. Bauer, A. Locatelli, S. Cherifi, and S. Heun, J. Phys. IV **132**, 159 (2006).
[16]R. Engel-Herbert, D. M. Schaadt, S. Cherifi, E. Bauer, R. Belkhou, A. Locatelli, S. Heun, A. Pavlovska, J. Mohanty, K. H. Ploog, and T. Hesjedal, J. Magn. Magn. Mater. **305**, 457 (2006).
[17]R. Engel-Herbert, A. Locatelli, S. Cherifi, D. M. Schaadt, J. Mohanty, K. H. Ploog, E. Bauer, R. Belkhou, S. Heun, A. Pavlovska, T. Leo, and T. Hesjedal, Appl. Phys. A **84**, 231 (2006).
[18]Y. Takagaki, B. Jenichen, C. Herrmann, E. Wiebicke, L. Däweritz, and K. H. Ploog, Phys. Rev. B **73**, 125324 (2006).
[19]M. Tortarolo, M. Sirena, J. Milano, L. B. Steren, F. Vidal, B. Rache Salles, V. H. Etgens, M. Eddrief, G. Faini, and L. I. Pietrasanta, Phys. Rev. B **81**, 224406 (2010).
[20]M. Tortarolo, F. Fernandez Baldis, M. Sirena, L. B. Steren, J. Milano, V. H. Etgens, M. Eddrief, and G. Faini, J. Appl. Phys. **112**, 013915 (2012).
[21]A. Locatelli, L. Aballe, T. O. Menteş, M. Kiskinova, and E. Bauer, Surf. Interface Anal. **38**, 1554 (2006).
[22]T. O. Menteş, G. Zamborlini, A. Sala, and A. Locatelli, Beilstein J. Nanotechnol. **5**, 1873 (2014).
[23]A. Vansteenkiste, J. Leliaert, M. Dvornik, M. Helsen, F. Garcia-Sanchez, and B. Van Waeyenberge, AIP Adv. **4**, 107133 (2014).
[24]C. Favieres, J. Vergara, and V. Madurga, J. Phys.: Condens. Matter **25**, 066002 (2013).
[25]C. L. Dennis, R. P. Borges, L. D. Buda, U. Ebels, J. F. Gregg, M. Hehn, E. Jouguelet, K. Oundajela, I. Petej, I. L. Prejbeanu, and M. J. Thornton, J. Phys.: Condens. Matter **14**, R.1175 (2002).
[26]F. Schippan, G. Behme, L. Däweritz, K. H. Ploog, B. Dennis, K.-U. Neumann, and K. R. A. Ziebeck, J. Appl. Phys. **88**, 2766 (2000).
[27]A. Hubert and R. Shäfer, *Magnetic Domains* (Springer, 2008).
[28]F. Fernandez Baldis, M. Sirena, L. B. Steren, V. H. Etgens, M. Eddrief, C. Ulysse, and G. Faini, Appl. Phys. Lett. **107**, 012407 (2015).
[29]K.-S. Ryu, J. B. Kim, Y. P. Lee, H. Akinaga, T. Manago, R. Viswan, and S.-C. Shin, Appl. Phys. Lett. **89**, 232506 (2006).